ACSNANO
www.acsnano.org
ARTICLE

Constructing Fast Carrier Tracks into Flexible Perovskite Photodetectors To Greatly Improve Responsivity

Xiaoming Li,[†,‡,∥] Dejian Yu,[†,∥] Jun Chen,[†,∥] Yue Wang,[§] Fei Cao,[†] Yi Wei,[†] Ye Wu,[†] Lin Wang,[†] Ying Zhu,[†] Zhiguo Sun,[†] Jianping Ji,[†] Yalong Shen,[†] Handong Sun,[§] and Haibo Zeng*[,†,‡]

[†]MIIT Key Laboratory of Advanced Display Materials and Devices, Institute of Optoelectronics & Nanomaterials, College of Materials Science and Engineering, Nanjing University of Science and Technology, Nanjing 210094, China

[‡]State Key Laboratory of Mechanics and Control of Mechanical Structures, College of Materials science and Technology, Nanjing University of Aeronautics and Astronautics, Nanjing 210016, China

[§]Division of Physics and Applied Physics, School of Physical and Mathematical Sciences, Nanyang Technological University, 637371, Singapore

S *Supporting Information*

ABSTRACT: **Intrinsically high mobility and large absorption coefficient endow inorganic halide perovskites (IHPs) with great promise for high-performance photodetectors (PDs), which, however, are being hindered by the low carrier extraction and transport efficiency of the solution assembled films. Here, we report on a general strategy to enhance the perovskite film conductivity that carbon nanotubes (CNTs) conductive nanonets are constructed from to provide fast carrier tracks. Resultantly, the $CsPbBr_3$ nanosheet/CNT composite films exhibit both high light harvesting and high conductivity, such advantages are demonstrated by the high performances of corresponding planar PDs. Specifically, the highest external quantum efficiency (EQE) of 7488% and the highest responsivity of 31.1 A W^{-1} under a bias of 10 V among IHP PDs with planar structure are achieved, which are almost 125-fold over the previous best results. Besides, the efficient charge extraction and transport also remarkably contribute to the fast response speed where a rise time of 16 μs is achieved, which is also superior to state-of-the-art IHP PDs. Furthermore, the composite films exhibit impressive flexibility due to the ultrathin 2D and 1D structural characteristic of perovskites and CNTs. By deploying the PD as a point-like detector, we acquire clear images. The results indicate the promising potentials of the perovskite/CNT composites for solution and ambient condition processed flexible devices, and this strategy is general for all kinds of perovskite optoelectronic devices including photodetectors, phototransistors, and even LEDs.**

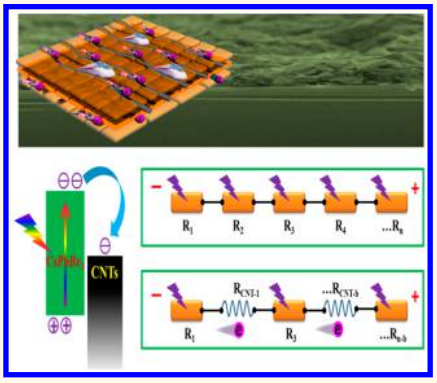

KEYWORDS: *fast carrier channel, carbon nanotube, perovskite, two-dimensional, photodetector*

All inorganic cesium lead halide perovskites (IHPs), a rising star in the perovskite family, have attracted great interest due to their fascinating chemical, optical, and semiconducting characteristics.[1−6] Particularly, IHP nanocrystals (NCs) were found to be highly luminescent with narrow emission bandwidth and flexible bandgap tunability, indicating their potential applications in light-emitting diodes (LEDs) for high-quality lighting and display.[1,7−12] Besides, research including applications in photodetectors (PDs), transistors, memristors, and lasers with solution processed strategies has also soared.[2,7,13−17] For most of the applications, IHPs show outstanding performances, though most of them were assembled with solution methods. In contrast, planar PDs based on IHPs only exhibit mediocre performance,[18] though they are claimed to own both a high absorption coefficient (~2× 10^5 cm^{-1})[3] and large carrier mobility (1000 cm^2 V^{-1} s^{-1}),[19,20] which are much higher than those of the famous 2D MoS_2 and comparable to those of Si.[21,22] One of the most critical reasons for the poor performances can be the low conductivity of solution assembled IHP films.

Due to the low solubility of IHP precursors, one-step processed IHP films exhibit poor continuity and limited thickness controllability.[12,23] Therefore, nanostructure dispersions are usually applied for device fabrications due to their controllable concentration (thickness), facile film fabrication

Received: December 7, 2016
Accepted: January 20, 2017
Published: January 20, 2017

DOI: 10.1021/acsnano.6b08194
ACS Nano XXXX, XXX, XXX−XXX

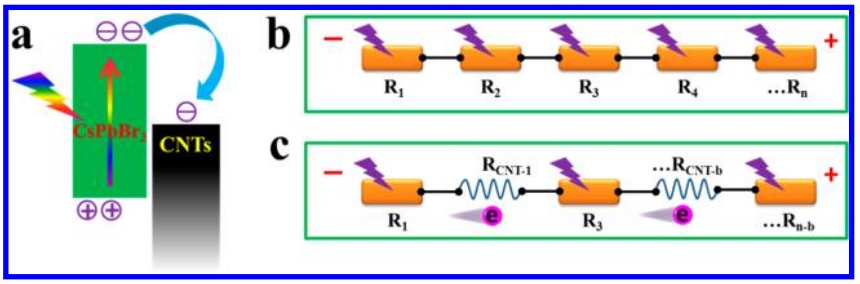

Figure 1. (a) Energy level of $CsPbBr_3$ nanosheets and CNTs. Simplified circuit diagrams of (b) the pristine $CsPbBr_3$ nanosheet PDs and (c) the hybrid PDs.

(compact films), and freedom from substrate. However, first, during the film fabrication, the fast evaporation of solvents usually destroys the film continuity. Second, to obtain considerable dispersivity, surfactants are inevitable, which form drifting obstacles for electrons between nanostructures. As a result, nanoparticle films show a low conductivity which dark current down to pA scale is frequently obtained and the photocurrent is usually as low as nA.[14,24,25] Oriented nanostructures with high crystallinity, such as nanowires and two-dimensional (2D) nanosheets, were synthesized to achieve better film conductivity.[18,26−28] Nonetheless, the photoresponse behavior is still far from practical applications. To obtain high-performance planar structure PDs, superior film quality and enhanced conductivity will benefit them greatly,[29] while, to the best of our knowledge, no related work has been reported to date for IHPs.

In this work, we introduce a general strategy to enhance the film conductivity of perovskites and hence boost their performance in optoelectronic devices. Conductive nanonets were constructed in perovskite films with carbon nanotubes (CNTs) to provide fast carrier tracks, and $CsPbBr_3$ nanosheets were chosen as examples. The main concept of the strategy is shown in Figure 1a−c where two dominating factors contribute to the improvements. First, according to the energy level of $CsPbBr_3$ nanosheets and CNTs,[15] photogenerated electrons will be extracted quickly to CNTs. Such an efficient electron extraction will result in a fast response speed and efficient usage of excited electrons (Figure 1a). Second, the separated film building blocks, such as nanocrystals, nanowires, and nanosheets, can be recognized as independent unit devices. For such photoconductive PDs, the total film resistance can be calculated to be $R_1 + R_2 + \cdots + R_n$ (Figure 1b). In contrast, when electrons transport to CNTs, they can drift along the CNTs smoothly due to the high conductivity of CNTs (Figure 1c). Compared to the active semiconductors, the resistance of CNTs can be neglected. Therefore, the total resistance of the composite film is $R_1 + R_2 + \cdots + R_{n-b}$ (Figure 1c), which is much smaller than pristine films. Then, the responsivity and external quantum efficiency (EQE) of PDs should be improved, owing to the efficient charge extraction and transport. Factually, CNTs can be recognized as inside electrodes, which possess a much smaller (down to nanometers, Figure 1c) distance compared to the macroscopic devices (tens of microns). Therefore, the transit time will be reduced, leading to a faster response speed and low recombination rate. Totally, such a strategy will contribute to both high response speed and high responsivity.

As a result, the $CsPbBr_3$ nanosheet/CNT composite films exhibit high conductivity as expected, which was demonstrated by the high performances of corresponding planar PDs. Specifically, the highest EQE of 7488% and the highest responsivity of 31.1 A W^{-1} under a bias of 10 V among IHP PDs with planar structure were achieved, which were almost 125-fold over previous best results. Besides, efficient charge extraction and transport contribute to a fast response speed, and a rise time of 16 μs was achieved, which was also superior to state-of-the-art IHP PDs. The decay time is 0.38 ms, which is also faster than most of the previous IHP PDs. The composite films exhibit impressive flexibility due to the ultrathin 2D and 1D structural characteristic of perovskite and CNT, which the PDs exhibit good flexibility (>10000 bending cycles) and photostability (<3.8% after 10000 on/off switching cycles). By deploying the PD as a point-like detector, we acquire clear images.[30] The results indicate the promising potentials of the $CsPbBr_3$ nanosheet/CNT composites for solution and ambient conditions processed flexible devices, and this strategy is general for many kinds of perovskite optoelectronic devices.

RESULTS AND DISCUSSION

The morphology and structural properties of the applied $CsPbBr_3$ nanosheets are shown in Figure 2a, which exhibit a lateral size of several microns. Though the morphology of nanosheet is not very uniform, no obvious byproducts such as

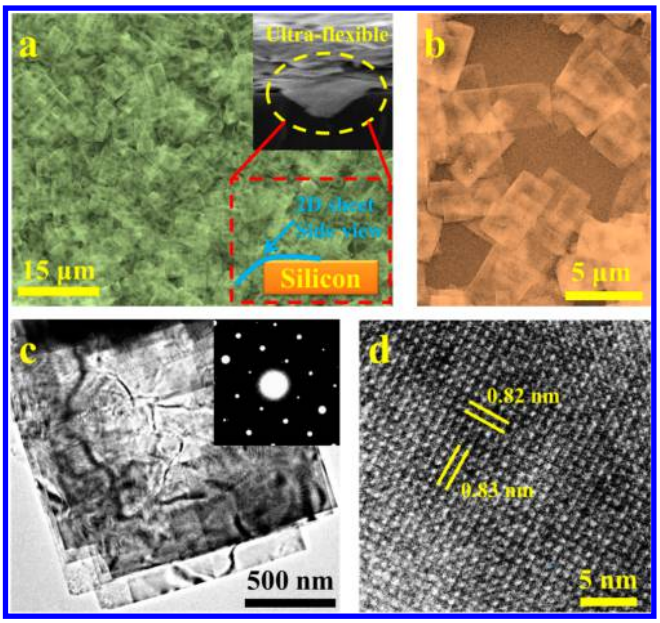

Figure 2. (a) SEM image of the $CsPbBr_3$ nanosheet. The inset shows the side view of the film. (b) High-magnification SEM image of the $CsPbBr_3$ nanosheets. (c) TEM image of the nanosheets. The inset in (c) shows the SAED pattern of the nanosheets. (d) High-resolution TEM images of the $CsPbBr_3$ nanosheets.

DOI: 10.1021/acsnano.6b08194
ACS Nano XXXX, XXX, XXX−XXX

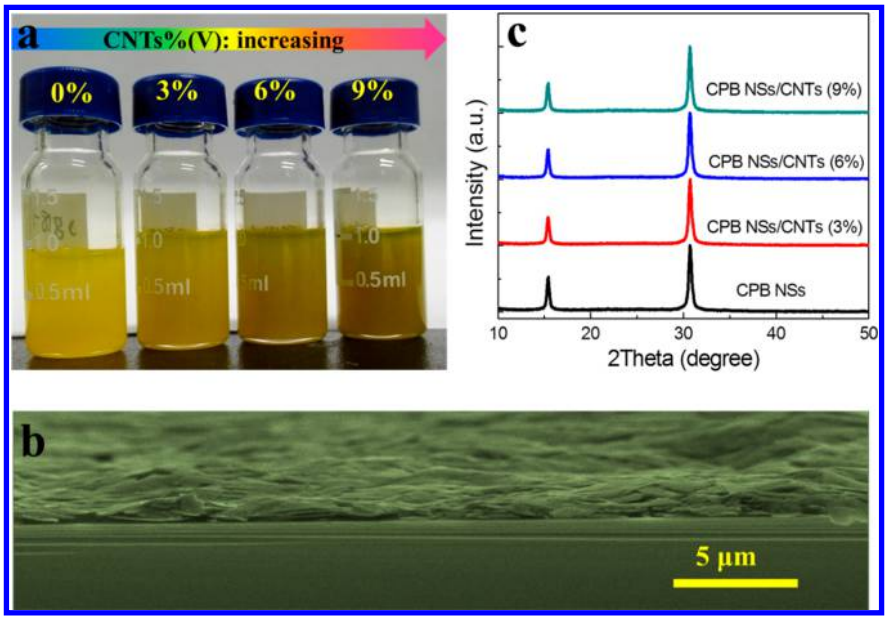

Figure 3. (a) Photograph of the dispersions with different amount of CNTs. (b) Cross-section SEM image of the composite film. (c) XRD results of the films with different amount of CNTs.

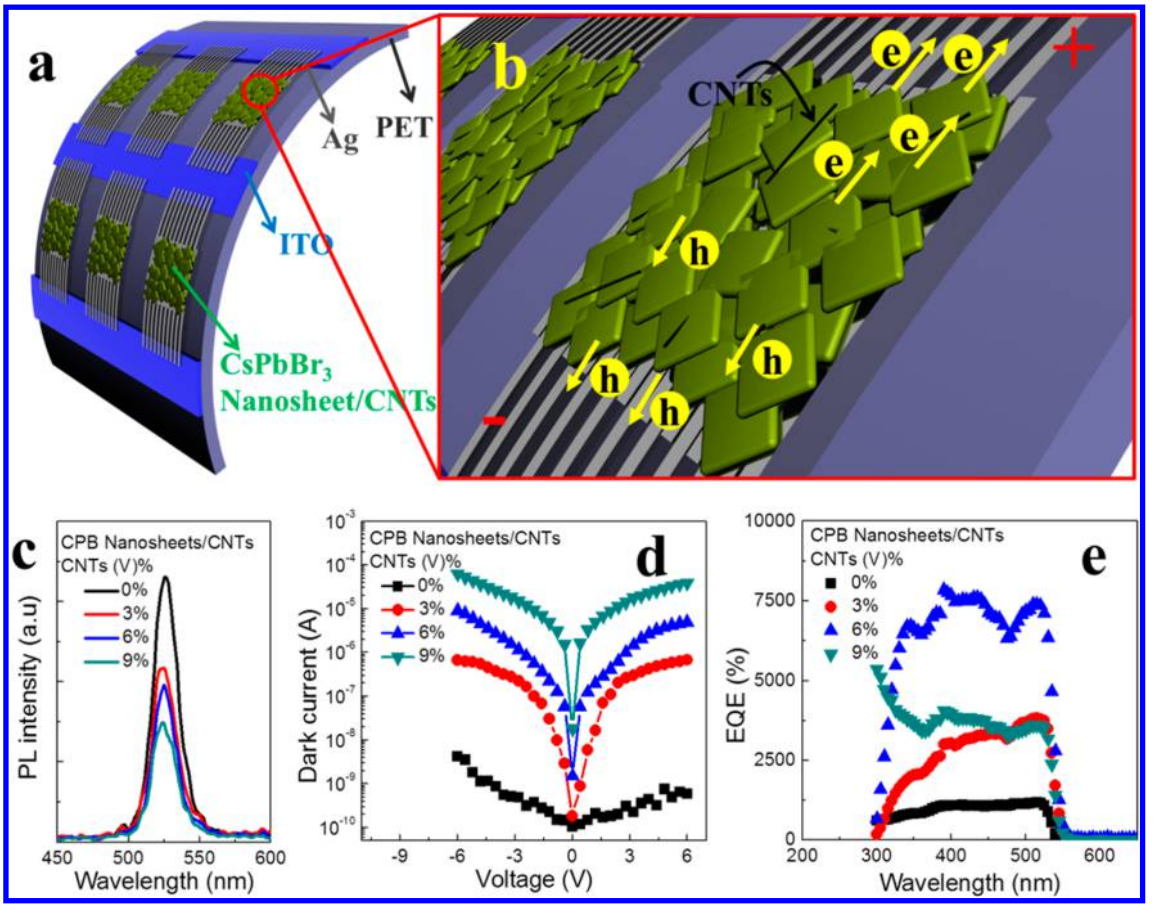

Figure 4. (a) Schematic illustration of the flexible PD. (b) Enlarged schematic illustration of the film consists of $CsPbBr_3$ nanosheet and CNTs. (c) PL spectra of the $CsPbBr_3$ nanosheet with different amount of CNTs. (d) Dark logarithmic $I-V$ curves of the PDs with different amount of CNTs. (e) EQE results of devices with different amounts of CNTs under a bias of 10 V. In all the figures, $CsPbBr_3$ is abbreviated as CPB.

particles are observed. EDX result of the $CsPbBr_3$ nanosheets informs that the atomic ratio of the elements is nearly 1:1:3 (Figure S1). They tend to lie in the substrate and then assemble into compact films due to the structural features of large nanosheets (an average area of ~26 μm^2, Figure S2) and relatively good dispersity with small amounts of residual

DOI: 10.1021/acsnano.6b08194
ACS Nano XXXX, XXX, XXX−XXX

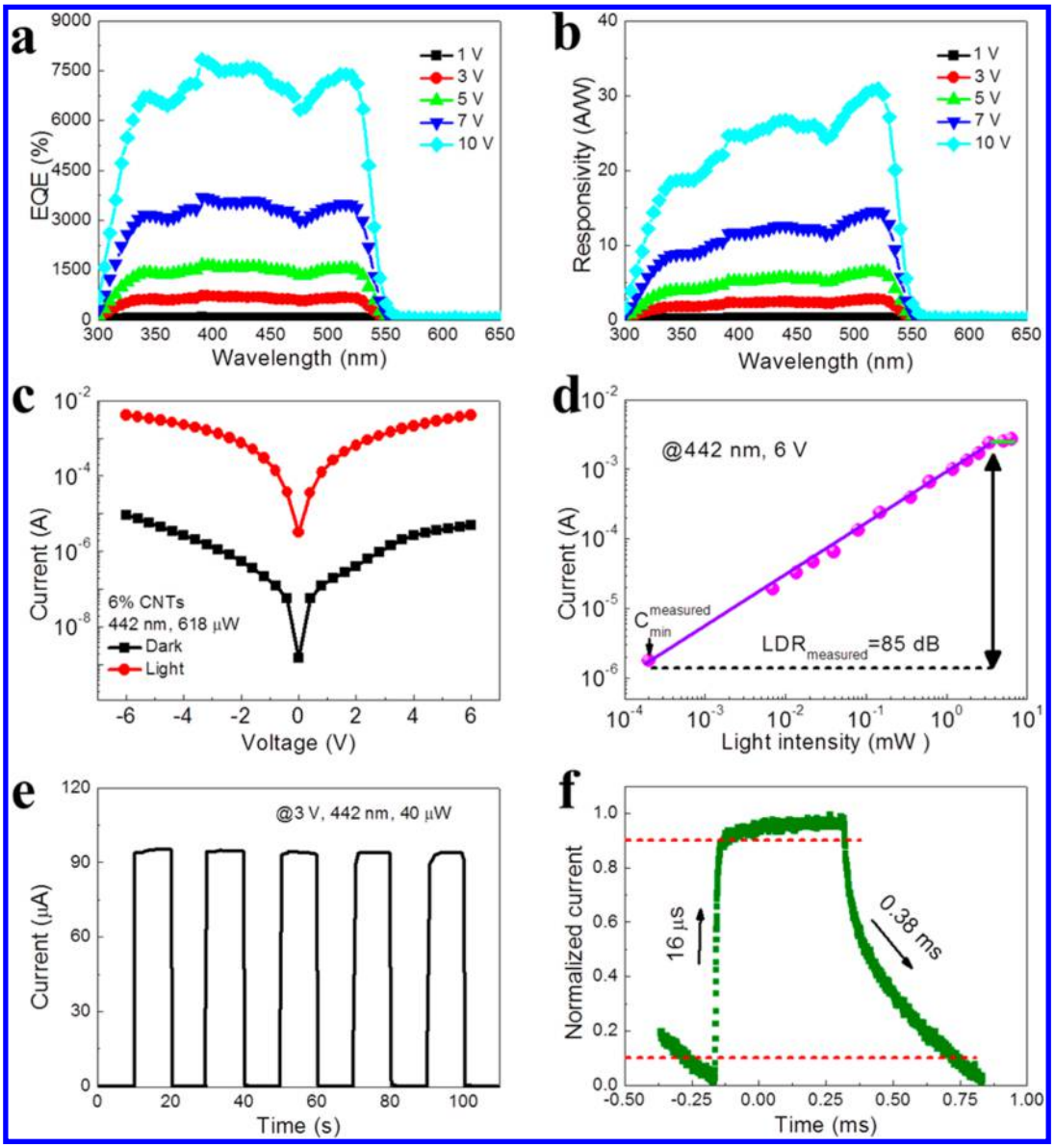

Figure 5. (a) EQE and (b) responsivity spectra under different biases. (c) Logarithmic *I*–*V* curves under dark and 442 nm light illumination. (d) Photocurrent *versus* light intensity of the PD under 442 nm light illumination. (e) *I*–*t* curve of the PD at 3 V under 442 nm. (f) Rise and decay time of the device at a frequency of 500 Hz.

ligands. At the overlaps of nanosheets, we can see the under sheets through the upper ones (Figure 2b). The high transparency implies the ultrathin thickness of the $CsPbBr_3$ nanosheets, which was confirmed to be 19 nm by AFM measurements (Figure S3). Such thickness insures high crystallinity and few defects, which is favorable to charge transport. Additionally, the nanosheets exhibit intrinsic and excellent flexibility, bending naturally when at the edge of a substrate (shown in Figure 2a inset). The schematic of side-view is also shown to demonstrate the bent behavior. Figure 2c shows the TEM results of the nanosheets. The observed wrinkle of the nanosheets indicates the good flexibility and thin thickness, which is consisted with other 2D materials such as graphene and MoS_2 and so on. Several nanosheets stack together, and we can also see the under nanosheets, which agrees well with the SEM images. No connection is observed along the nanosheets, indicating the single crystallinity. This is also confirmed by the corresponding SAED pattern in Figure 2c inset. The HRTEM images in Figure 2d show interplanar spacing of ~0.82 and 0.83 nm, which are related to the lattice of orthorhombic phase of $CsPbBr_3$ (a = 0.8207 nm, b = 0.8255 nm, c = 1.1759 nm).[27]

The conductive tracks were constructed during a film formation process by adding CNTs into $CsPbBr_3$ nanosheet dispersions directly, and the films in this work were all prepared by drop-casting. Before dropping, the composite dispersions were ultrasonicated for 30 min. The fast evaporation of solvent prevents the precipitation of CNTs, forming a uniform composite films.

Figure 3a shows the photograph of the $CsPbBr_3$ nanosheet dispersions with various amounts of CNTs. The as-prepared $CsPbBr_3$ nanosheets were divided into four equal parts. Then, CNTs/toluene dispersion was added to these samples according to the volume ratio of 0, 3, 6, and 9% to fabricate films with different conductivity. With the increase of CNTs, the dispersions become darker, which exhibit good dispersity

DOI: 10.1021/acsnano.6b08194
ACS Nano XXXX, XXX, XXX–XXX

after sonication, ensuring good film formation ability. Therefore, the composite films can be fabricated with drop casting or spin coating strategies. Thanks to the structure features of nanosheets and CNTs, they tend to stack layer by layer into high-quality, dense, and crack-free films, as shown by the SEM image in Figure 3b. To gain more insights into the features of assembled films after the addition of CNTs, XRD measurements were conducted. The feature of the films does not show obvious change, but possesses apparent orientated behavior (Figure 3c). Two sharp and strong diffraction peaks are observed, which confirms the 2D structure, orientated assembly, and high crystallinity of $CsPbBr_3$ nanosheets and the films. The peak at ~30.73° corresponds to the (220) plane of orthorhombic $CsPbBr_3$ structure, which agrees well with the TEM results. CNTs do not influence the film formation process, but only constructing conductive tracks within films. Besides, owing to the single crystallinity and facile solution procedures, the $CsPbBr_3$ nanosheet/CNT composite dispersions are expected to exhibit high performances in flexible PDs.

The flexible electrodes and PDs based on $CsPbBr_3$ nanosheet/CNT composite films are illustrated in Figure 4. It is worth noting that all the procedures were conducted under ambient conditions, including the preparation of nanosheets and fabrication of electrodes (Figure S4). The laser printed electrodes exhibit straight and uniform stripes, free from connecting and discontinuity. The optimized electrodes possess an interval of 16 μm, which is small enough for efficient transition of photogenerated carriers (Figure S4). Figure 4a demonstrates the schematic of the device structure that active composite films are deposited by drop-casting onto the as-fabricated flexible substrate. The film thickness is controlled through adjusting dispersion concentration or casting times, and the CNTs were embedded in $CsPbBr_3$ nanosheets. Under bias, photogenerated carriers are expected to separate and transport to electrodes quickly (Figure 4b).

To investigate the influence of the addition of CNTs on films, basic optical and electronic properties were measured. One can see that the PL intensity of composite films decreases gradually with the increase of CNTs, which might be assigned to the efficient extraction of excited electrons (Figure 4c). This is also confirmed by the decreased PL lifetime in samples with more CNTs, as shown in Figure S6. The conductive CNT nanonets with an appropriate energy lever lead to fast extraction of electrons (Figure 1a). The excited electrons contribute to photocurrent more, while only some of them recombine to emit light at the beginning, resulting in a fast lifetime. This is consistent with the results in Figures 4c and 1a that when most of the electrons are extracted and transport through films smoothly, PL intensity will decrease. A large amount of CNTs also contributes to the decrease of optical absorption (Figure S7).

With the increase of CNTs, the dark current of these PDs shows an enhancement of more than 3 orders of magnitude, which increases from 10^{-9} to more than 10^{-5} A at 3 V (Figure 4d). If we calculate the resistance simply according to the Ohm's law, it decreases from 1 GΩ to 0.1 MΩ. Therefore, as expected (Figure 1c), owing to the high conductivity of CNTs, fast tracks for carrier transport formed, and the film conductivity was improved significantly. Obviously, photogenerated carriers will be extracted quickly and efficiently, which can drift through the film smoothly. By virtue of the intrinsic flexibility of materials and substrate, as well as the high conductivity of the composite films, fast response speed and high quantum efficiency are expected.

Figure 4e shows the EQE spectra as a function of the wavelength of the devices under a bias of 10 V. First, we want to emphasize that though materials are fabricated at room temperature, the PDs based on only $CsPbBr_3$ nanosheets exhibited good performance compared to previous reports with IHPs, and the same device construction that the EQE reaches to ~1169% (Figure 4e).[14,15,24,31] Due to the low dark current and efficient electron transport, the current at a bias of 6 V increased from 5.9×10^{-10} to 7.8×10^{-4} A under the illumination of 442 nm laser light (618 μW), exhibiting an on/off ratio of more than 10^5 (Figure S8). Increased amounts of CNTs contribute to a higher EQE that when the volume ratio increased to 6%, an EQE of 7488% was achieved. Compared to the bare $CsPbBr_3$ nanosheets, the addition of CNTs results in an EQE increase of more than 6300%, which is nearly 125-fold over the previously best results.[15] According to the definition of EQE, such improvement mainly results from the enhanced film conductivity, carrier extraction, and carrier transport. However, too many CNTs result in decreased EQE (Figures 5e and S10), which might be derived from weakened light absorption (Figure S7). Moreover, high dark current results from a large amount of CNTs lead to low on/off ratio, which decreases from 10^5 to ~90.

Then, considering all the parameters including EQE, responsivity, and switching ratio, we made detailed investigations on the device with 6% CNTs. Figure 5 shows the performances of the photoconductive detector based on a $CsPbBr_3$ nanosheet/CNT (6%) composite, which exhibits almost the best responsivity among PDs based on IHPs. With the increase of applied bias, both the EQE and responsivity increase monotonously (Figure 5a,b). The responsivity of 31.1 A W^{-1} obtained at a bias of 10 V is much higher than that of commercial Si PDs with a similar device structure (<0.2 A W^{-1}).[32,33] Under the illumination of 442 nm light, the photocurrent can reach up to ~4 mA under a bias of 6 V, indicating an on/off ratio of more than 823 (Figure 5c). The photocurrent increases drastically with the increase of bias, demonstrating a nonlinear $I-V$ behavior of Schottky contact between composite films and electrodes.

The photoresponse characteristics under different illumination intensities were examined as shown in Figure S11. The linearity of photoresponse to light intensity is very important for practical and high-contrast applications during further signal/information processing. Figure 5d shows that the PDs possess a broad linear dynamic range (LDR), which can be calculated according to following eq 1, where L is the input light intensity. The upper and lower limit currents are obtained within the linear results. Figure 5d shows a linear response from 0.5 μW to 3.38 mW, corresponding to a LDR of 85 dB (at +6 V). When the light intensity is larger than 3.38 mW, the current increase rate slows. the detection limit is almost 0.5 μW, and the switching ratio is only about 10. This result is much higher than that of the commonly used InGaAs PDs.

$$\mathrm{LDR} = 20\log\frac{L_{\mathrm{upper}}}{L_{\mathrm{lower}}} \quad (1)$$

To illustrate the photoswitching behavior of the CNT-doped PDs, the 442 nm light was shut and shed periodically during the measurement of current. Figure 5e shows the $I-t$ curve under a bias of 3 V and light intensity of 40 μW. Upon turning on the

DOI: 10.1021/acsnano.6b08194
ACS Nano XXXX, XXX, XXX−XXX

Table 1. Performance Comparisons of Pervoskite PDs from Previous Reports about Lateral Device Structures Based on Both Hybrid and Inorganic Perovskites

active materials	EQE (%)	responsivity (A W^{-1})	rise/decay time (ms)	refs
$CsPbBr_3$ microparticles	42	0.18	1.8/1.0	14
$CsPbI_3$ NCs	–	–	24/29	24
$CsPbBr_3$ nanosheet	–	–	17.8/14.7	
$CsPbBr_3$ nanoparticles/Au NCs	40	0.01	0.2/1.2	31
$CsPb(Br/I)_3$ nanorods	–	–	680/660	36
$CsPbBr_3$ 2D nanosheet	53	0.25	0.019/0.025	15
$MAPbI_3$ nanoparticles	1190	3.49	100/100	37
$MAPbI_3$ (network)	–	0.1	0.3/0.4	38
TiO2-$MAPbI_3$	–	0.00049	20/20	39
$MAPbBr_3$ single crystal film	$>10^6$	4×10^3	0.025/0.025	34
$MAPbI_3$ nanowires	–	5×10^{-3}	0.5/0.5	40
$MAPbI_3$ nanowires	–	1.32	0.3/0.3	41
$MAPbI_3$ microwires	–	13.5	0.08/0.24	42
$(RNH_3)_2(CH_3NH_3)_{n-1}M_nX_{3n+1}$	–	0.013	10/7.5	43
$CsPbBr_3$ nanosheets/CNTs	**7488**	**31.1**	**0.016/0.38**	**this work**

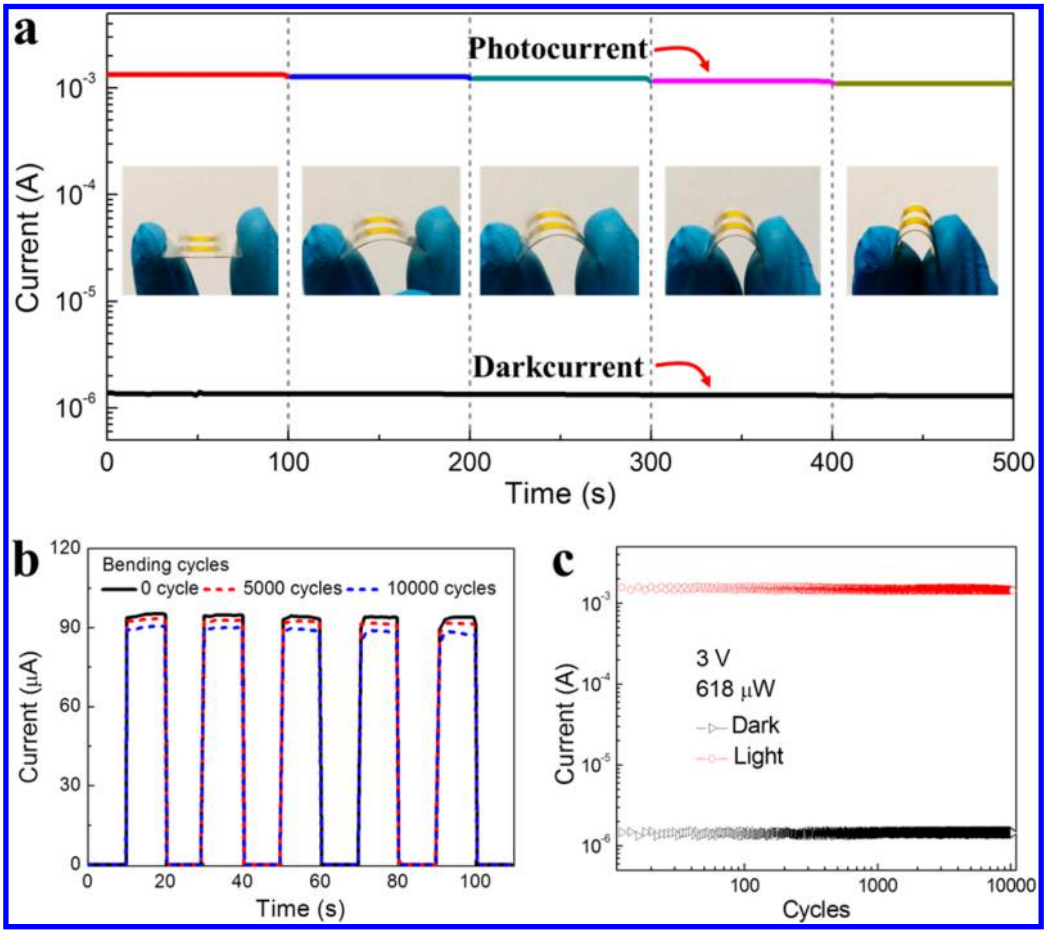

Figure 6. (a) Current of the flexible device with various bending radii at a bias of 3 V. (b) *I*–*t* curves of the device with different bending–recovering cycles. (c) Photo and dark current after more than 10000 cycles under 3 V bias with 442 nm light (618 μW) illumination.

light, the current sharply rises, which can be as high as ~100 μA. When the light is sheltered, the current falls fast, implying the fast response of the PDs. The device exhibits a reproducible photocurrent in response to the on/off light cycles. The response speed was measured with a continuous 442 nm laser light triggered by a tunable pulse generation (Figure 5f). The rise and decay times measured under a pulse frequency of 500 Hz were 16 μs and 0.38 ms, respectively, which are much shorter than those reported in nanoparticle or small 2D IHP nanosheet based devices, and the rise time is more than 100-fold shorter than that of the device without CNTs (Figure S12).[14,24,31] The fast response speed indicates the fast separation and efficient extraction of photogenerated carriers, which can be attributed to the improved conductivity with CNTs.

DOI: 10.1021/acsnano.6b08194
ACS Nano XXXX, XXX, XXX–XXX

Many works have been reported on the photoconductive devices based on varied material morphologies including nanoparticles, nanosheets and single crystals of both inorganic and hybrid halide perovskites. Some of them exhibit good performances regarding with EQE, responsivity, and on/off ratio, as shown in Table 1. One can see that except for the device based on $MAPbBr_3$ single crystal films, the as-fabricated device shows the best performance.[34] Specifically, for IHP-based PDs, an enhancement of ~125-fold in EQE or responsivity is achieved compared with previous best results. Meanwhile, the rise time is superior to state-of-the-art IHP PDs. The slow decay time can be attributed to the fast tracks for carrier transport from the doping of CNTs, which makes carrier transport smoothly, with little scattering and recombination. The device performance is expected to be further modulated with gate voltage due to the facile processability. Most importantly, all the procedures are carried out under ambient conditions, without any heating and annealing, indicating their huge potential in low-cost and high-quality flexible or even wearable PDs.

Regarding the intrinsic flexibility of the thin nanosheets (Figure 2a) and the film structure, the stress can be released efficiently during bending, which make them more suitable for flexible optoelectronic devices compared to nanoparticle or bulk form. Additionally, the long CNTs act as rebar in concrete, which are also flexible and do not influence the strength of the films at all. In contrast, they will render excellent mechanical flexibility for these flexible devices.[35] The ultraflexible characteristic of the 2D structure and enhanced mechanical flexibility by CNTs ensure a good retention rate during bending.

The photocurrent stability of the device is measured at different bending radii under illumination of 442 nm light to evaluate the device performance (Figure 6a). No obvious change is observed under different bending states, which implies that the device performance remains unchanged with external bending stress. Figure 6b depicts the $I-t$ curves before and after bending for different times, and the device was controlled by an oscillator. Remarkably, after continuous bending and recovering for more than 10000 times, the photocurrent changes from 95 to 89 μA, exhibiting an extreme stability that a decrease of ~6.4% is obtained. In addition to the small current fluctuation, the response speed is not influenced greatly, either. Furthermore, to evaluate the operation stability, photocurrent was recorded under continuous light on/off switching (618 μW) at 3 V for more than 10000 cycles (Figure 6c). Both the photo- and dark current almost remain unchanged, and the deterioration is smaller than 3.8%, suggesting the composite film based PDs have excellent stability.

In addition to communication, another important application of PDs is imaging. A brief introduction of the homemade measurement system is shown in Figure 7a. First, laser light passed through a beam expander to form a diverging light. Then this light illuminated on a mask with letters of NUST (Nanjing University of Science and Technology). The as-fabricated PD controlled by stepping motor behind the mask scans step by step along x and y axes with a step size of 2 mm. The current under a bias of 3 V was detected by a Keithley 2400 device. Sites with light will exhibit a higher current, while other dark places will show a lower current. As a result, the logo is clearly represented, as shown in Figure 7b. Though the imaging results are not perfect, *i.e.*, the strokes are not straight or round, they can be improved *via* decreasing the device size and increasing pixels.

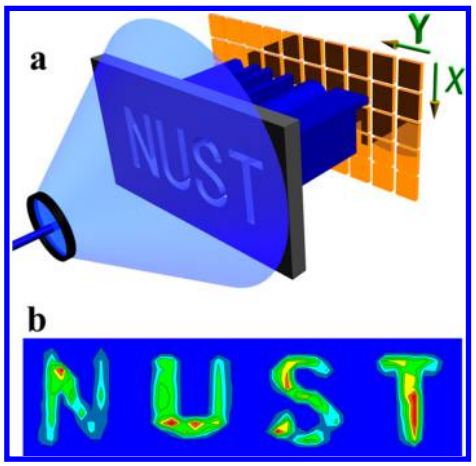

Figure 7. (a) Schematic demonstration of the imaging system. (b) Imaging results of Nanjing University of Science and Technology logo. Reprinted with permission. Copyright, Nanjing University of Science and Technology.

CONCLUSION

By constructing conductive carrier tracks within $CsPbBr_3$ nanosheet films using CNTs, totally highly conductive composite films were obtained. Consequently, high-performance PDs with EQE and responsivity as high as 7488% and 31.1 A W^{-1} were fabricated. Besides, efficient charge extraction and transport contribute to a fast response speed, and a rise time of 16 μs was achieved. All the results are superior to state-of-the-art IHP PDs with a planar device structure. The introduction of CNTs ensures excellent mechanical strength, which the PDs exhibit good flexibility and photostability. By deploying the PD as a point-like detector, we acquire clear images.[30] This work opens the window for the fabrication of perovskite films with high conductivity and then improved device performance. The strategy is universal that in addition to CNTs, many other materials are favorable, such as metal nanoparticels, nanowires, graphene, and so on so forth, indicating the promising applications of this method in high-performance communication devices, imaging devices, and LEDs with halide perovskites. Besides, the introduction of CNTs can also modify the film formation process of one-step solution processed IHP films by providing heterogeneous nucleation seeds and increasing solution concentration. In addition to CNTs, semiconductor nanomaterials are also favorable for specific design and applications with this strategy.

EXPERIMENTAL SECTION

Preparation of $CsPbBr_3$ Nanosheet/CNT Dispersions. All of the reagents were purchased from Aladdin and were used directly without purification. All of the procedures were conducted under ambient conditions. First, 0.1 mL of precursor (1 mmol CsBr and 0.5 mmol of $PbBr_2$ were dissolved in 14 mL of DMSO and 1 mL HAc) and 0.5 mL of ligands (2 g of octadecaylamine dissolved in 10 mL HAc) were mixed and stirred for 2 min. Then 10 mL toluene was added and stirred for another 5 min. The reaction was stopped by centrifugation of 5000 rpm/1 min. After that, the precipitation was redispersed in toluene and washed one more time to rule out the residual ligands and byproducts, which was finally dispersed in 4 mL of toluene. 1 mL of the $CsPbBr_3$ nanosheets was mixed with 30, 60, and 90 μL of CNT dispersion, respectively (1.6 mg of CNTs in 4 mL of

DOI: 10.1021/acsnano.6b08194
ACS Nano XXXX, XXX, XXX−XXX

toluene, ultraconicated for 3 h), which was sonicated for 30 min before use.

Fabrication and Measurements of Flexible PDs. Commercial Ag nanoparticle ink was spin-coated onto the prepatterned ITO/PET substrate. Then the as-prepared film was illuminated with a focused 405 nm laser controlled by stepping motors to prepare interdigital electrodes. The width and interval of the electrodes were modulated by laser energy and scanning rate. PDs were fabricated by drop-casting the $CsPbBr_3$ nanosheet/CNT dispersion on the electrodes. The EQE and responsivity of PDs were characterized with a Zolix DSR-101-UV system equipped with a Si PD as reference. On/off cycling performances and response speed were measured with a continuous semiconductor laser (442 nm) and a trigger under different pulse width equipped with an oscilloscope. All the current results were measured with Keithley 2400 and Keithley 6487.

Material Characterizations. Absorption properties of films were measured with a Shimadzu 3600 UV−vis spectrophotometer. Photoluminescence spectra were measured using a Varian Cary Eclipse instrument. XRD patterns were recorded on Bruker D8 Advance. TEM and HRTEM measurements were implemented with FEI Tecnai G20 on a Cu grid. SEM images were measured with FEI Quanta 250F field emission electron microscope. The thicknesses of electrode and nanosheets were detected with an AFM system, Bruker Multimode 8. The PL lifetime was detected and analyzed by an Optronics streak camera system with optimized temporal resolution of ≈50 ps.

ASSOCIATED CONTENT

Supporting Information

The Supporting Information is available free of charge on the ACS Publications website at DOI: 10.1021/acsnano.6b08194.

Figures S1−S12 (SEM, AFM, and detailed photodetector results) (PDF)

AUTHOR INFORMATION

Corresponding Author

*E-mail: zeng.haibo@njust.edu.cn.

ORCID

Haibo Zeng: 0000-0002-7132-8885

Author Contributions

‖These authors contributed equally.

Notes

The authors declare no competing financial interest.

ACKNOWLEDGMENTS

This work was financially supported by the National Key Basic Research Program of China (2014CB931702), NSFC (51572128, 21403109), NSFC-RGC (5151101197), the National Key Research and Development Program of China (2016YFB0401701), the Fundamental Research Funds for the Central Universities (nos. 30915012205, 30916015106), Natural Science Foundation of Jiangsu Province (BK20140769), PAPD of Jiangsu Higher Education Institutions, and in the USA by DoD (grant W911NF-15-1-0650)

REFERENCES

(1) Protesescu, L.; Yakunin, S.; Bodnarchuk, M. I.; Krieg, F.; Caputo, R.; Hendon, C. H.; Yang, R. X.; Walsh, A.; Kovalenko, M. V. Nanocrystals of Cesium Lead Halide Perovskites ($CsPbX_3$, X = Cl, Br, and I): Novel Optoelectronic Materials Showing Bright Emission with Wide Color Gamut. *Nano Lett.* **2015**, *15*, 3692−3696.

(2) Wang, Y.; Li, X.; Zhao, X.; Xiao, L.; Zeng, H.; Sun, H. Nonlinear Absorption and Low-Threshold Multiphoton Pumped Stimulated Emission from All-Inorganic Perovskite Nanocrystals. *Nano Lett.* **2016**, *16*, 448−453.

(3) De Roo, J.; Ibáñez, M.; Geiregat, P.; Nedelcu, G.; Walravens, W.; Maes, J.; Martins, J. C.; Van Driessche, I.; Kovalenko, M. V.; Hens, Z. Highly Dynamic Ligand Binding and Light Absorption Coefficient of Cesium Lead Bromide Perovskite Nanocrystals. *ACS Nano* **2016**, *10*, 2071−2081.

(4) Swarnkar, A.; Chulliyil, R.; Ravi, V. K.; Irfanullah, M.; Chowdhury, A.; Nag, A. Colloidal $CsPbBr_3$ Perovskite Nanocrystals: Luminescence Beyond Traditional Quantum Dots. *Angew. Chem., Int. Ed.* **2015**, *54*, 15424−15428.

(5) Wang, Y.; Li, X.; Sreejith, S.; Cao, F.; Wang, Z.; Stuparu, M. C.; Zeng, H.; Sun, H. Photon Driven Transformation of Cesium Lead Halide Perovskites from Few-Monolayer Nanoplatelets to Bulk Phase. *Adv. Mater.* **2016**, *28*, 10637−10643.

(6) Huang, H.; Polavarapu, L.; Sichert, J. A.; Susha, A. S.; Urban, A. S.; Rogach, A. L. Colloidal Lead Halide Perovskite Nanocrystals: Synthesis, Optical Properties and Applications. *NPG Asia Mater.* **2016**, *8*, e328.

(7) Li, X.; Wu, Y.; Zhang, S.; Cai, B.; Gu, Y.; Song, J.; Zeng, H. $CsPbX_3$ Quantum Dots for Lighting and Displays: Room-Temperature Synthesis, Photoluminescence Superiorities, Underlying Origins and White Light-Emitting Diodes. *Adv. Funct. Mater.* **2016**, *26*, 2435−2445.

(8) Song, J.; Li, J.; Li, X.; Xu, L.; Dong, Y.; Zeng, H. Quantum Dot Light-Emitting Diodes Based on Inorganic Perovskite Cesium Lead Halides ($CsPbX_3$). *Adv. Mater.* **2015**, *27*, 7162−7167.

(9) Zhang, X.; Lin, H.; Huang, H.; Reckmeier, C.; Zhang, Y.; Choy, W. C. H.; Rogach, A. L. Enhancing the Brightness of Cesium Lead Halide Perovskite Nanocrystal Based Green Light-Emitting Devices through the Interface Engineering with Perfluorinated Ionomer. *Nano Lett.* **2016**, *16*, 1415−1420.

(10) Ling, Y.; Tian, Y.; Wang, X.; Wang, J. C.; Knox, J. M.; Perez-Orive, F.; Du, Y.; Tan, L.; Hanson, K.; Ma, B.; Gao, H. Enhanced Optical and Electrical Properties of Polymer-Assisted All-Inorganic Perovskites for Light-Emitting Diodes. *Adv. Mater.* **2016**, *28*, 8983−8989.

(11) Huang, H.; Chen, B.; Wang, Z.; Hung, T. F.; Susha, A. S.; Zhong, H.; Rogach, A. L. Water Resistant $CsPbX_3$ Nanocrystals Coated with Polyhedral Oligomeric Silsesquioxane and Their Use As Solid State Luminophores in All-Perovskite White Light-Emitting Devices. *Chem. Sci.* **2016**, *7*, 5699−5703.

(12) Li, J.; Shan, X.; Bade, S. G. R.; Geske, T.; Jiang, Q.; Yang, X.; Yu, Z. Single-Layer Halide Perovskite Light-Emitting Diodes with Sub-Band Gap Turn-On Voltage and High Brightness. *J. Phys. Chem. Lett.* **2016**, *7*, 4059−4066.

(13) Wang, Y.; Li, X.; Song, J.; Xiao, L.; Zeng, H.; Sun, H. All-Inorganic Colloidal Perovskite Quantum Dots: A New Class of Lasing Materials with Favorable Characteristics. *Adv. Mater.* **2015**, *27*, 7101−7108.

(14) Li, X.; Yu, D.; Cao, F.; Gu, Y.; Wei, Y.; Wu, Y.; Song, J.; Zeng, H. Healing All-Inorganic Perovskite Films *via* Recyclable Dissolution−Recyrstallization for Compact and Smooth Carrier Channels of Optoelectronic Devices with High Stability. *Adv. Funct. Mater.* **2016**, *26*, 5903−5912.

(15) Song, J.; Xu, L.; Li, J.; Xue, J.; Dong, Y.; Li, X.; Zeng, H. Monolayer and Few-Layer All-Inorganic Perovskites As a New Family of Two-Dimensional Semiconductors for Printable Optoelectronic Devices. *Adv. Mater.* **2016**, *28*, 4861−4869.

(16) Meyns, M.; Perálvarez, M.; Heuer-Jungemann, A.; Hertog, W.; Ibáñez, M.; Nafria, R.; Genç, A.; Arbiol, J.; Kovalenko, M. V.; Carreras, J.; Cabot, A.; Kanaras, A. G. Polymer-Enhanced Stability of Inorganic Perovskite Nanocrystals and Their Application in Color Conversion LEDs. *ACS Appl. Mater. Interfaces* **2016**, *8*, 19579−19586.

(17) Wu, Y.; Wei, Y.; Huang, Y.; Cao, F.; Yu, D.; Li, X.; Zeng, H. Capping $CsPbBr_3$ with ZnO to Improve Performance and Stability of Perovskite Memristors. *Nano Res.* **2016**, DOI: 10.1007/s12274-016-1288-2.

(18) Lv, L. F.; Xu, Y. B.; Fang, H. H.; Luo, W. J.; Xu, F. J.; Liu, L. M.; Wang, B. W.; Zhang, X. F.; Yang, D.; Hu, W. D.; Dong, A. G. Generalized Colloidal Synthesis of High-Quality, Two-Dimensional

DOI: 10.1021/acsnano.6b08194
ACS Nano XXXX, XXX, XXX−XXX

Cesium Lead Halide Perovskite Nanosheets and Their Applications in Photodetectors. *Nanoscale* **2016**, *8*, 13589−13596.
(19) Stoumpos, C. C.; Malliakas, C. D.; Peters, J. A.; Liu, Z.; Sebastian, M.; Im, J.; Chasapis, T. C.; Wibowo, A. C.; Chung, D. Y.; Freeman, A. J.; Wessels, B. W.; Kanatzidis, M. G. Crystal Growth of the Perovskite Semiconductor $CsPbBr_3$: A New Material for High-Energy Radiation Detection. *Cryst. Growth Des.* **2013**, *13*, 2722−2727.
(20) Yettapu, G. R.; Talukdar, D.; Sarkar, S.; Swarnkar, A.; Nag, A.; Ghosh, P.; Mandal, P. Terahertz Conductivity within Colloidal $CsPbBr_3$ Perovskite Nanocrystals: Remarkably High Carrier Mobilities and Large Diffusion Lengths. *Nano Lett.* **2016**, *16*, 4838−4848.
(21) Jacoboni, C.; Canali, C.; Ottaviani, G.; Alberigi Quaranta, A. A Review of Some Charge Transport Properties of Silicon. *Solid-State Electron.* **1977**, *20*, 77−89.
(22) Kim, S.; Konar, A.; Hwang, W.-S.; Lee, J. H.; Lee, J.; Yang, J.; Jung, C.; Kim, H.; Yoo, J.-B.; Choi, J.-Y.; Jin, Y. W.; Lee, S. Y.; Jena, D.; Choi, W.; Kim, K. High-Mobility and Low-Power Thin-Film Transistors Based on Multilayer MoS_2 Crystals. *Nat. Commun.* **2012**, *3*, 1011.
(23) Yantara, N.; Bhaumik, S.; Yan, F.; Sabba, D.; Dewi, H. A.; Mathews, N.; Boix, P. P.; Demir, H. V.; Mhaisalkar, S. Inorganic Halide Perovskites for Efficient Light-Emitting Diodes. *J. Phys. Chem. Lett.* **2015**, *6*, 4360−4364.
(24) Ramasamy, P.; Lim, D.-H.; Kim, B.; Lee, S.-H.; Lee, M.-S.; Lee, J.-S. All-Inorganic Cesium Lead Halide Perovskite Nanocrystals for Photodetector Applications. *Chem. Commun.* **2016**, *52*, 2067−2070.
(25) Dong, Y.; Gu, Y.; Zou, Y.; Song, J.; Xu, L.; Li, J.; Xue, J.; Li, X.; Zeng, H. Improving All-Inorganic Perovskite Photodetectors by Preferred Orientation and Plasmonic Effect. *Small* **2016**, *12*, 5622−5632.
(26) Zhang, D.; Eaton, S. W.; Yu, Y.; Dou, L.; Yang, P. Solution-Phase Synthesis of Cesium Lead Halide Perovskite Nanowires. *J. Am. Chem. Soc.* **2015**, *137*, 9230−9233.
(27) Shamsi, J.; Dang, Z.; Bianchini, P.; Canale, C.; Stasio, F. D.; Brescia, R.; Prato, M.; Manna, L. Colloidal Synthesis of Quantum Confined Single Crystal $CsPbBr_3$ Nanosheets with Lateral Size Control up to The Micrometer Range. *J. Am. Chem. Soc.* **2016**, *138*, 7240−7243.
(28) Zhang, D.; Yang, Y.; Bekenstein, Y.; Yu, Y.; Gibson, N. A.; Wong, A. B.; Eaton, S. W.; Kornienko, N.; Kong, Q.; Lai, M.; Alivisatos, A. P.; Leone, S. R.; Yang, P. Synthesis of Composition Tunable and Highly Luminescent Cesium Lead Halide Nanowires Through Anion-Exchange Reactions. *J. Am. Chem. Soc.* **2016**, *138*, 7236−7239.
(29) Liu, X.; Wang, C.; Xiao, X.; Wang, J.; Guo, S.; Jiang, C.; jong Yu, W.; Hu, W.; Li, J.; Liao, L. High Mobility Amorphous InGaZnO Thin Film Transistor with Single Wall Carbon Nanotubes Enhanced-Current Path. *Appl. Phys. Lett.* **2013**, *103*, 223108.
(30) Engel, M.; Steiner, M.; Avouris, P. Black Phosphorus Photodetector for Multispectral, High-Resolution Imaging. *Nano Lett.* **2014**, *14*, 6414−6417.
(31) Dong, Y.; Gu, Y.; Zou, Y.; Song, J.; Xu, L.; Li, J.; Xue, J.; Li, X.; Zeng, H. Improving All-Inorganic Perovskite Photodetectors by Preferred Orientation and Plasmonic Effect. *Small* **2016**, *12*, 5622−5632.
(32) Lee, H. C.; Van Zeghbroeck, B. A Novel High-Speed Silicon MSM Photodetector Operating at 830 nm Wavelength. *IEEE Electron Device Lett.* **1995**, *16*, 175−177.
(33) Laih, L.-H.; Chang, T.-C.; Chen, Y.-A.; Tsay, W.-C.; Hong, J.-W. Characteristics of MSM Photodetectors With Trench Electrodes on p-type Si Wafer. *IEEE Trans. Electron Devices* **1998**, *45*, 2018−2023.
(34) Saidaminov, M. I.; Adinolfi, V.; Comin, R.; Abdelhady, A. L.; Peng, W.; Dursun, I.; Yuan, M.; Hoogland, S.; Sargent, E. H.; Bakr, O. M. Planar-Integrated Single-Crystalline Perovskite Photodetectors. *Nat. Commun.* **2015**, *6*, 8724.
(35) Liu, X.; Wang, C.; Cai, B.; Xiao, X.; Guo, S.; Fan, Z.; Li, J.; Duan, X.; Liao, L. Rational Design of Amorphous Indium Zinc Oxide/Carbon Nanotube Hybrid Film for Unique Performance Transistors. *Nano Lett.* **2012**, *12*, 3596−3601.
(36) Tang, X.; Zu, Z.; Shao, H.; Hu, W.; Zhou, M.; Deng, M.; Chen, W.; Zang, Z.; Zhu, T.; Xue, J. All-Inorganic Perovskite $CsPb(Br/I)_3$ Nanorods for Optoelectronic Application. *Nanoscale* **2016**, *8*, 15158−15161.
(37) Hu, X.; Zhang, X.; Liang, L.; Bao, J.; Li, S.; Yang, W.; Xie, Y. High-Performance Flexible Broadband Photodetector Based on Organolead Halide Perovskite. *Adv. Funct. Mater.* **2014**, *24*, 7373−7380.
(38) Deng, H.; Yang, X.; Dong, D.; Li, B.; Yang, D.; Yuan, S.; Qiao, K.; Cheng, Y.-B.; Tang, J.; Song, H. Flexible and Semitransparent Organolead Triiodide Perovskite Network Photodetector Arrays with High Stability. *Nano Lett.* **2015**, *15*, 7963−7969.
(39) Xia, H.-R.; Li, J.; Sun, W.-T.; Peng, L.-M. Organohalide Lead Perovskite Based Photodetectors with Much Enhanced Performance. *Chem. Commun.* **2014**, *50*, 13695−13697.
(40) Horváth, E.; Spina, M.; Szekrényes, Z.; Kamarás, K.; Gaal, R.; Gachet, D.; Forró, L. Nanowires of Methylammonium Lead Iodide ($CH_3NH_3PbI_3$) Prepared by Low Temperature Solution-Mediated Crystallization. *Nano Lett.* **2014**, *14*, 6761−6766.
(41) Deng, H.; Dong, D.; Qiao, K.; Bu, L.; Li, B.; Yang, D.; Wang, H.-E.; Cheng, Y.; Zhao, Z.; Tang, J.; Song, H. Growth, Patterning and Alignment of Organolead Iodide Perovskite Nanowires for Optoelectronic Devices. *Nanoscale* **2015**, *7*, 4163−4170.
(42) Deng, W.; Zhang, X.; Huang, L.; Xu, X.; Wang, L.; Wang, J.; Shang, Q.; Lee, S.-T.; Jie, J. Aligned Single-Crystalline Perovskite Microwire Arrays for High-Performance Flexible Image Sensors with Long-Term Stability. *Adv. Mater.* **2016**, *28*, 2201−2208.
(43) Zhou, J.; Chu, Y.; Huang, J. Photodetectors Based on Two-Dimensional Layer-Structured Hybrid Lead Iodide Perovskite Semiconductors. *ACS Appl. Mater. Interfaces* **2016**, *8*, 25660−25666.

DOI: 10.1021/acsnano.6b08194
ACS Nano XXXX, XXX, XXX−XXX